

Original scientific paper

**INVESTIGATION OF INFLUENCES OF FABRICATION
TOLERANCES ON OPERATIONAL CHARACTERISTICS OF
PIEZO-ACTUATED STICK-SLIP MICRO-DRIVES**

Xuan-Ha Nguyen, Hung-Anh Nguyen

Department of Machine Design and Robotics, School of Mechanical Engineering,
Hanoi University of Science and Technology, Hanoi, Vietnam

Abstract. *Piezo-actuated stick-slip micro-drives (PASSMDs) are often used in microrobotic applications due to their advantages of a straightforward design and good operational characteristics. In this work, influences of fabrication tolerances on operational characteristics of PASSMDs are theoretically investigated. A dynamic model describing the whole macroscopic movement of the driver's runner and the actuators, and the microscopic behavior of the frictional contacts using the method of dimensionality reduction, was used. Three essential parameters of the drives including the angle between working surfaces of the runner, the alignment angle between two actuator blocks on each side of the runner, and the stiffness of an individual actuator, whose values are impacted by the tolerance of the fabrication and assembly process, were considered as the input of the investigation. By performing hybrid-dynamic simulations, influences of these parameters on the drives' operational characteristics, including the repeatability of the step length, the critical amplitude phenomenon, and the maximal-achievable driving frequency/velocity, were evaluated. Simulation results show that these parameters significantly influence on the characteristics of the drives. The contribution of this work is so important that several important phenomena of PASSMDs, which are experimentally detected, are physically explained for the first time. The results of this work could help designers to optimize for better generations of PASSMDs.*

Key words: *Microrobotics, Stick-slip micro-drivers, Piezo actuators, Contact mechanics, Dynamic simulation, Friction*

Received March 11, 2021 / Accepted April 12, 2021

Corresponding author: Xuan-Ha Nguyen

Department of Machine Design and Robotics, School of Mechanical Engineering, Hanoi University of Science and Technology, Hanoi 112452, Vietnam

E-mail: ha.nguyenxuan@hust.edu.vn

1. INTRODUCTION

For many techniques of the micro-system technology and the microrobotics, a need for small-scale ultra-high-precision positioning and manipulation devices is extremely necessary [1]. These devices are required to generate motions with a traveling range of several centimeters and a very high resolution of sub micrometer or several ten nanometers. Additionally, the devices must operate in special working environments, which are usually small-space, clean and high-rate of vacuum. Therefore, the miniaturization and the dust-free capability are also considered.

Piezo-actuated stick-slip micro-drives (PASSMDs) are a very good candidate to solve the requirements mentioned above. PASSMDs have a very simple design consisting of a mobile part (the runner) guided and actuated by the piezo actuators (the actuator) through frictional guiding contacts attached to the piezo elements [2]. Motions of the runner are induced by the deformation of the piezo elements usually supplied by sawtooth-like driving voltages. These motions consist of a sequence of stick and slip phases. During the stick phase, the piezo elements are slowly elongated, which makes the runner to move slowly along with the actuator due to the static friction in the contacts between the runner's surfaces and the guides of the actuator. This phase is followed by the slip phase when the piezo elements are rapidly contracted. The runner cannot follow this movement and thus slides relatively with respect to the actuators. Subsequently, after a small backward motion (back-step), a step of the runner is achieved. Although the deformation of the piezoelectric element is small, this principle of motion allows for movements of the runner with a theoretically unlimited range by performing many cycles of the stick and slip phase (stepping mode). Also, motions with a very high resolution are obtained by a slight deformation of the piezo elements within the stick phase (scanning mode).

There have been many prototypes as well as commercial products of PASSMDs released [3]. Also, many theoretical investigations and optimizations for drives have been published [4, 5]. Important research and development topics are briefly summarized as follows:

- *Design and miniaturization*: the monolithic concept for modular drives to reduce efforts of assembling micro-components [6], exploitation of the flexure-based mechanism for adjusting the preload and thus the friction with the aim of increasing step length and load capacity [7],
- *Waveform and driving electronics optimization*: new driving waveforms for maximal velocity [8-10], optimized driving electronics for reducing the slew-rate and thus increasing the step length and velocity [11],
- *Physical modeling and simulation*: modeling the friction in the guiding contacts using Coulomb model [12, 13], single state friction model [14-16], tangential contact mechanics with the method of dimensionality reduction for hybrid dynamic simulations [3, 10, 17-20].

Among these topics, the physical modeling is the most important because it can theoretically explain important characteristics of the stick-slip drives experimentally detected such as: i) the so-called 0-amplitude [10, 19, 21] /critical amplitude [20] which relates directly to the presliding displacement of guiding contacts and the dynamic behavior of the piezo actuators. The state-of-the-art explanation for this phenomenon can be found in [20]; ii) the micro-vibration and the maximal achievable driving frequency [10, 20]; iii) The repeatability – an evaluation criterion for the changing of the step length after each

step which is believed to relate to the tolerance of the fabrication and assembly of micro-components of the drives. This phenomenon has not been physically analyzed yet.

The fabrication tolerance is determined by the micro-machining of micro-parts as well as their assembly processes typically performed in manual ways. This leads to the fact that the tolerance of manufactured drives is very fluctuated, influencing significantly on the operational characteristics of the drives. To our knowledge, there has not been any investigation considering the influences of fabrication tolerances on operational characteristics of PASSMDs.

In this work, the influences of fabrication tolerances on the above-mentioned operational characteristics of the PASSMDs are theoretically investigated. Based on previously published works [10, 18-20], an experimental platform having a linear stick-slip micro-drive, in which a runner is guided and driven by six piezo-actuators, was illustrated. A hybrid-dynamic model [10, 18-20], which allows us to simulate the overall macroscopic movements of the runner and the microscopic behavior of guiding contacts, was used. The angle between the working surfaces of the runner, the alignment angle between two actuator blocks, and the stiffness and damping ratio of an individual actuator, which are impacted by the fabrication and assembly tolerances, were considered. Influences of these parameters on operational characteristics of the drive, including the fluctuation of the step length, the critical amplitude and the maximal achievable driving frequency are analyzed and presented.

2. EXPERIMENTAL IMPLEMENTATION

2.1. Experimental platform

The experimental platform used in this work is the result of the work of Edeler [16] and the adaption of our previously published works [3, 10]. Some measurement results of these works are shown in this paper for the first time. For the convenience of readers, a brief description of the system is presented.

The investigated drive is a linear micro-positioning device. The device consists of a runner which is guided and driven by six piezoelectric micro-actuators, as shown in Fig. 1. Each actuator is constructed by a ruby hemisphere glued on segments of a structured piezo element. These actuators are arranged on both sides of the runner, four actuators on the left and two actuators on the right (see Figs. 1b, c). In each side of the runner, the actuators are aligned to each other with an angle of 90° . With this arrangement, the runner can perform horizontally translational forward and backward movements. The actuator holder on the right is fixed to the housing, while the left one is movable and guided by a very low-friction linear ball bearing. Preloads applied to the drive are generated and regulated by a spring-system acting on the left actuator holder. The value of preloads is measured by a force sensor (M17 by ATI Industrial Automation, Pinnacle Park Apex, NC, USA). The position of the runner is measured via a high-resolution laser interferometer (SP-120 by SIOS Meßtechnik GmbH, Ilmenau, Germany). In the runner's movement direction, a miniature load cell (M31 by Sensing and Control Automation and Control Solutions Honeywell, Golden Valley, MN, USA) is set up in front of the runner to measure forces generated by the drive. When the runner touches the load cell, the force is measured and recorded.

The piezo elements are supplied by saw-tooth like driving voltages whose amplitude, slew-rate and frequency can be varied via driving electronics. When six synchronous saw-tooth like driving voltages are applied to the piezo elements, the six hemispheres also performed synchronous saw-tooth like displacements, leading to stick-slip motions for the

runner. The displacement amplitude of the contact center of each ruby hemispheres/actuator is denoted as the actuation amplitude. This amplitude depends on the radius of the hemispheres, the dimension and the structure of the piezo, as well as the amplitude of driving voltages. The radius of hemispheres, the driving frequency, the amplitude of driving voltages and the preload are varied to characterize the drive's behavior. In this work, the radii of the ruby hemispheres of 0.25mm , 0.5mm and 1mm are considered.

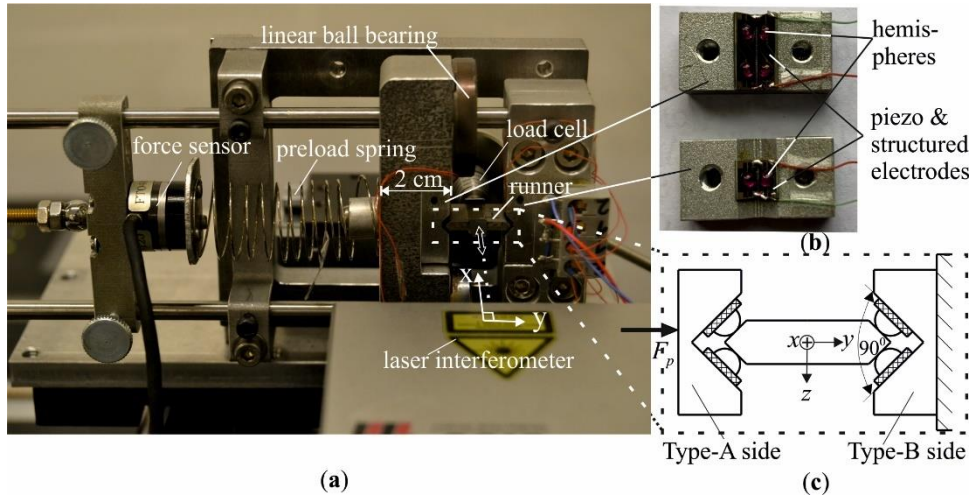


Fig. 1 Setup of the experimental platform: (a) photo of the test stand; (b) Photo of the piezo actuators; (c) CAD-based schematic front-view [16,10]

2.2. Fabrication and assembly tolerance

The investigated drive was fabricated and assembled manually, which could make the tolerance of the fabrication and the assembly of micro-parts vary in an uncontrollable manner. The structure of the piezo elements and the assembly of the actuators are schematically shown in Fig. 2. The piezo elements are fabricated out of a piezoceramic bulk (PIC151) via the laser-based micro-machining. There are two types of the structured piezo. The so-called “A-type” has two segment zones where two ruby hemispheres are glued on. The “B-type” has only one segment zone with one glued hemisphere (see also Fig. 1b). Each block of the piezo element and the ruby hemispheres are then glued to the actuator holders. For each actuator holder, the two blocks must align together with an angle of 90° . To our practical experiences, the fabrication and the manual assembly of such micro-parts are complicated and thus, the tolerance can vary in a large range. This makes the operational characteristics of the drive case-by-case very different.

Error resources determining the tolerance of the investigated drive are caused by both the fabrication and the assembly as follows:

- For the fabrication: the laser-based micro-machining method cannot ensure the depth of the groove of the piezo elements equal. This makes the dynamic behavior (stiffness and damping coefficients) of an individual actuator different from others. Also, the discrepancy of the displacement amplitude of the actuators appears. The fabrication of the runner also has variation.

- For the assembly: i) In fact, the ruby hemispheres are manually attached to the piezo elements using a glued layer under the support of a light microscope. The thickness and the configuration of the glue layer can randomly vary and cannot be well controlled. The configuration and the thickness of the glue layer between the ruby hemisphere and the piezo element, and their relative position, are proved to strongly impact the stiffness and the displacement amplitude of the actuators [21]. Therefore, discrepancies in the stiffness and the displacement amplitude among actuators are visible; ii) the geometrical errors caused by the assembly of each block of actuators and their attachment to the actuator holder, can change the contact angle and contact point between the hemisphere of the actuator and the runner's surfaces (see Fig. 2b). This leads to discrepancies in the displacement amplitude of the actuators as well as the normal force pressed on each contact.

In this work, influences of the discrepancy of stiffness/damping, the displacement amplitude among actuators, and the normal force of each contact on operational characteristics of the investigated drive are modelled and simulated.

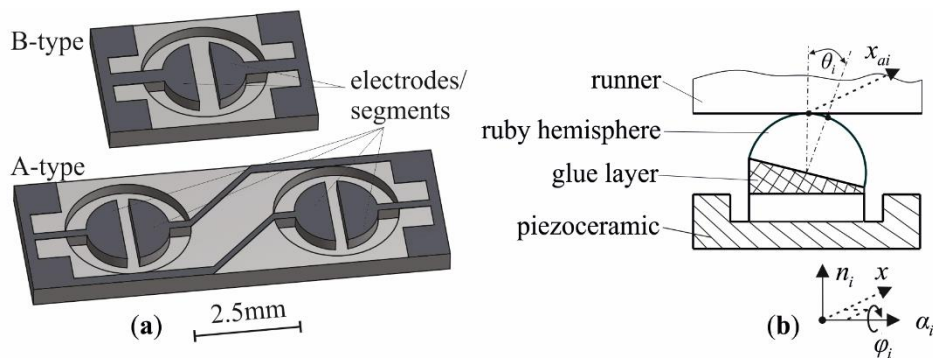


Fig. 2 CAD-based schematic view of actuator design: (a) the structured piezo; (b) The assembly of the actuators [3]

2.3. Measurement results

The experimental results shown in Fig. 3 are presented in this paper for the first time. The graphs present measurements of the step length of the runner at different contact positions between the runner's surfaces and the actuators. The level of the preload is also varied. For each level of the preload, measurements of ten measured positions are randomly chosen to be drawn. Fig. 3a presents data with the case of the radius of the ruby hemispheres $R = 1mm$ and Fig. 3b for $R = 0.25mm$. In Fig. 3a, with the case $R = 1mm$ and the level of the preload $F_p = 0.2N$, the discrepancy between the maximal step length and the minimal one is $22nm$ while the average of the step length is $149nm$. The maximal standard deviation is 8.6%. For the higher preload $F_p = 1N$ the discrepancy of the step length increases with the standard deviation of 13.4%. Thus, for this case the repeatability is reduced. In Fig. 3b, for the case $R = 0.25mm$ and $F_p = 0.5N$, the repeatability of the step length is very low. The measured step lengths have a large discrepancy with a maximum of $35nm$ in an average of $47.2nm$. The maximal standard deviation is 41.3%. With $F_p = 0.2N$, the repeatability is better.

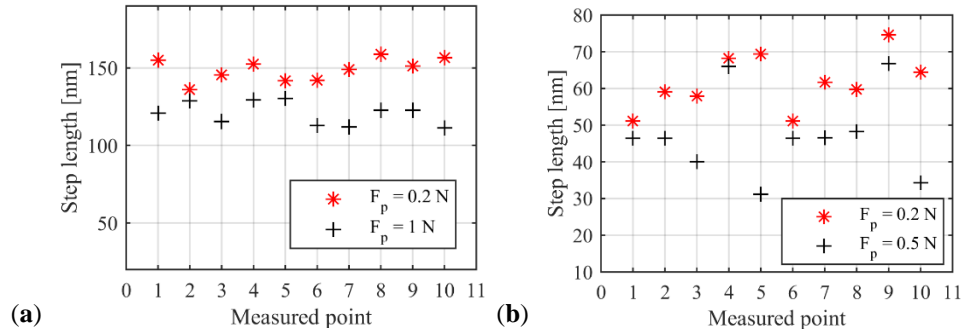


Fig. 3 The repeatability of the step length: (a) $R = 1 \text{ mm}$; (b) $R = 0.25 \text{ mm}$

In Fig. 4, the dependency of the critical amplitude on the preload for different ruby hemispheres radii is presented. We consider the error bar in the graphs. It is visible that the error bar becomes larger when the level of the preload increases. Also, if the radius of the ruby hemispheres is reduced, the error bar increases slightly. Experimental evidence shows that with the case $R = 0.25 \text{ mm}$ and the preload higher than 0.5 N the repeatability of the measurement is very low even the runner cannot perform a reliable movement. A maximal discrepancy between measured values of the critical amplitude is 8.2% at a preload of 0.5 N and $R = 0.25 \text{ mm}$, and 6.8% at a preload of 1.2 N and $R = 1 \text{ mm}$.

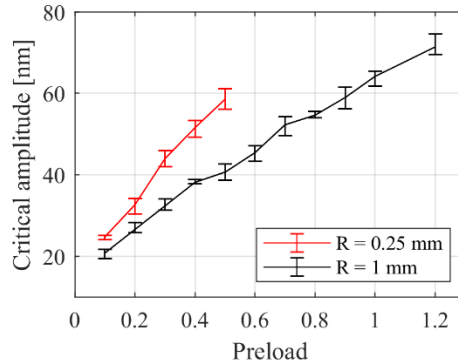


Fig. 4 The repeatability of critical amplitude depending on the preload for different ruby hemispheres radii

Fig. 5 shows the measurement of the runner's velocity which depends on the driving frequency for the case the radius of the ruby hemispheres $R = 0.5 \text{ mm}$ and a preload $F_N = 0.4 \text{ N}$. At each represented point, an error bar is shown which presents the repeatability of ten measurements. The driving frequency is varied in a range from 4.72 to 34.66 kHz . It is clearly seen that the runner's velocity increases with rising driving frequencies. When the driving frequency reaches to a value of 26 kHz , the velocity of the runner is maximal at a value of 1.76 mm/s with a standard deviation of 7.4%. If the driving frequency continues increasing, the velocity decreases gradually. This can be explained that, with driving frequencies higher than a maximal-achievable value, after each slip phase of the runner,

the micro-vibration cannot be damped before the runner starts the next stick-phase. As a result, chaos appears which leads to reductions in the runner's velocity. It is also seen that the higher the driving frequency is, the larger the error bar is. The repeatability of the runner's velocity reduces with the rising driving frequency.

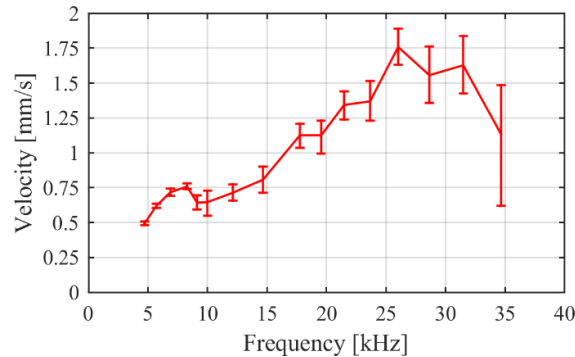


Fig. 5 The repeatability of runner's velocity depending on the driving frequency with a radius of the ruby hemispheres $R = 0.5mm$ and a preload $F_p = 0.4N$

We come to the following comments:

- Due to the fabrication and assembly tolerance of the actuators and the runner, discrepancies among actuators appear, including the stiffness/damping coefficients, the actuation amplitude, as well as the normal force of the guiding contacts. During the operation, the dynamic behavior of an individual actuator and thus the contact force are changed which influences the repeatability of the overall movement of the runner;
- The impact of fabrication and assembly tolerance on the repeatability becomes larger when the size of the system is decreased, and the preload and the driving frequency rise.

3. MODELING AND SIMULATION

3.1. Modeling

The concept of the hybrid dynamic simulation for PASSMDs was first proposed in [18] and further validated in [3, 10, 19, 22]. The basic idea of the concept is the combination of the macroscopic movement of the runner and the actuators with the microscopic behavior of the guiding contacts using the so-called method of dimensionality reduction [17]. In these works, the authors modeled the actuators as ideally rigid. The dynamic behavior of the actuators was not considered. Recently, in [20], the authors extended the model so that the actuators are considered as mass-spring-damper systems. However, all these works assume that the fabrication and assembly tolerance do not influence the characteristics of the drive. Therefore, discrepancies in the actuators' dynamic behavior and actuation amplitude and the contact forces were not modeled. In this work, we continue extending the model proposed in [20] so that the discrepancies caused by the fabrication and assembly tolerance are considered.

The extended macroscopic model to describe the investigated drive's overall movement is presented in Fig. 6 where a free-body diagram is drawn. The runner has a mass of m_r ,

whose movements in the horizontal direction are described by the coordinate x_r , under the acting of the normal and friction forces of the guiding contacts. In Fig. 6a, three mass-spring-damper systems of actuators are drawn where each system is depicted for two actuators (two at the top and four at the bottom). Unlike previously published work [20], in this work, due to the fabrication and assembly tolerance, dynamic parameters of the actuators as well as the contacting forces are not identical. Therefore, each actuator is modeled by a mass m_{ai} , a stiffness k_{pi} and a damping c_{pi} . Displacements of the actuators are described by x_{ai} . The deformation of the piezo elements is x_{pi} has a form of saw-tooth like as shown in Fig. 6c. For each contact, the normal and friction force are presented by F_{Ni} , and F_{fi} ($i = 1 \div 6$), respectively. The stiffness of the load cell is presented by k .

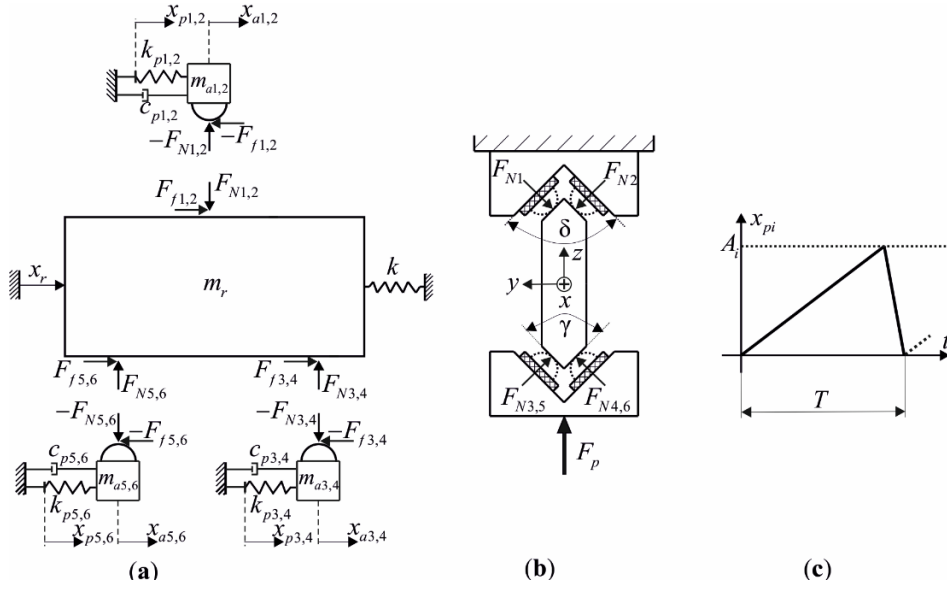


Fig. 6 Macroscopic modeling for the investigated drive

Macroscopic movements of the runner and the actuators are formulated via the Newtonian mechanics, in which Eq. 1 for the runner and Eq. 2 for the actuators. It is noticed that the influence of the gravity force is neglected [10]. The friction forces F_{fi} in Eqs. (1) and (2) are modelled by a microscopic model using MDR [17] which depends directly on the contact mechanics and the normal forces. Since the fabrication and assembly tolerance is considered, the modeling of them is additionally implemented.

$$m_r \ddot{x}_r = -kx_r + \sum_{i=1}^6 F_{fi} \quad (1)$$

$$m_{ai} \ddot{x}_{ai} = k_{pi}(x_{pi} - x_{ai}) - c_{pi}\dot{x}_{ai} - F_{fi} \quad (i = 1 \div 6) \quad (2)$$

Variations of the actuation amplitude of the contact points and the normal force applied on each contact, caused by the fabrication and assembly tolerance, are modeled as in Fig. 7.

- Firstly, the fabrication and assembly error of the actuator blocks are modeled in Figs. 7a and 7c. Fig. 7a depicts the ideal case when the actuator blocks are aligned together with an angle 90° (the continuous, black line) and the manufactured case. The fabrication and assembly tolerance are considered (the dashed, red line) where the alignment angle is not 90° but rather δ . Thus, the contact point between the ruby hemisphere and the runner's surface is shifted from the top of the ruby hemisphere C_i to C'_i determined by θ_i . As shown in Fig. 7c, in the direction of the movement x , when one ruby hemisphere is rotated with a displacement φ_i around α_i , the translational displacement of C_i and C'_i are x_{ai} and x'_{ai} respectively, whose relation is followed by the Eqs. (3) and (4). Thus, the actuation amplitude of the actual contact point A'_i can be smaller than the amplitude of the ideal case A_i determined by the variation of δ around 90° . In this case, the normal forces applied to the contacts remain unchanged.

$$\begin{cases} x_{ai} = R\varphi_i \\ x'_{ai} = R'_i\varphi_i \end{cases} \Rightarrow x'_{ai} = x_{ai} \cos \theta_i \Rightarrow A'_i = A_i \cos \theta_i \quad (3)$$

$$\theta_i = \left| \frac{\delta}{2} - 45^\circ \right| \quad (4)$$

- Secondly, the fabrication tolerance of the runner is considered. In fact, the runner's surfaces are not perfectly flat and geometrically accurate. As shown in Fig. 7b, the angle between the two working surfaces of the runner is modeled by γ . This angle is changed around 90° . For this case, the actual contact point is not C_i but rather C'_i (the dashed, red line for the real situation). Similarly, the actuation amplitude of the contact point is changed and determined by Eqs. (3) and (5). Consequently, compared to the ideal case with $\gamma = 90^\circ$, the actual normal forces applied in each

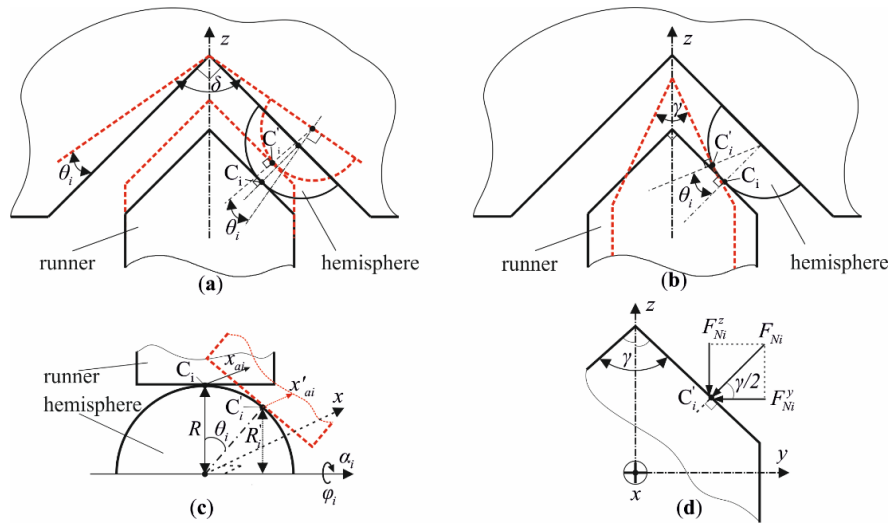


Fig. 7 Modeling of the influence of the fabrication and assembly tolerance on actuation amplitudes and normal forces

contact F_{Ni} ($i = 1 \div 6$) are formulated by Eq. (6), where F_{Ni}^z ($i = 1 \div 6$) are the projection of F_{Ni} on the z direction; F_p presents for the preload (see Fig. 7d).

$$\theta_i = \left| \frac{\gamma}{2} - 45^\circ \right| \quad (5)$$

$$\begin{cases} F_{Ni} = \frac{F_{Ni}^z}{\sin\left(\frac{\gamma}{2}\right)} \\ F_{N1}^z + F_{N2}^z = F_{N3}^z + F_{N4}^z + F_{N5}^z + F_{N6}^z = F_p \end{cases} \quad (6)$$

The friction forces F_{fi} ($i = 1 \div 6$) in Eqs. (1) and (2) can be modeled and calculated via the MDR [17]. Since this model was already described in detail in previously published works [3, 10, 18-20, 22]. Thus, we only briefly present the theory in this paper. Fig. 8b shows an equivalent one-dimensional contact model from the original three-dimensional model (Fig. 8a), where the elastic space is replaced by an elastic foundation with a set of springs. These springs have normal stiffness Δk_z and tangential stiffness Δk_x , which are chosen according to the following rules:

$$\Delta k_z = E^* \Delta x; \Delta k_x = G^* \Delta x, \quad (7)$$

where Δx is the distance between the spring, and E^* and G^* are respectively the equivalent elastic and shear modulus. The radius of the one-dimensional profile R_1 must be:

$$R_1 = \frac{R}{2}. \quad (8)$$

Using this simplified model, the dynamically changing contact area is estimated and thus, the friction force is computed. At each instant of time t of a dynamic simulation, the changing stick and slip area of the contact is determined by the state of the springs in the contact and the friction force is calculated as follows:

$$F_{fi}(t) = \sum_{j=1}^N f_{x,j}(t), \quad i = 1 \div 6, \quad (9)$$

where $f_{x,j}(t)$ is the tangential force of the springs in the contact, whose value depends on the state of each spring (stick or slip) related to the normal force F_{Ni} ; N is the number of springs in contact i .

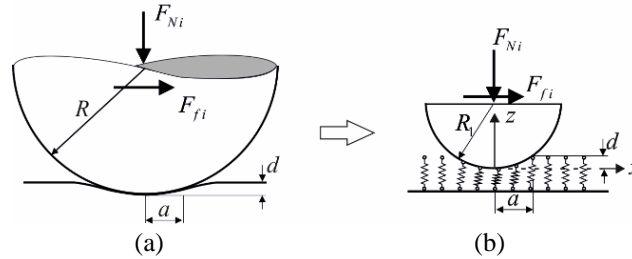


Fig. 8 Modeling of the micro-contact using MDR: a) three-dimensional contact model; b) one-dimensional contact model via MDR [17, 18]

3.2. Hybrid dynamic simulation

Simulations were performed using a hybrid dynamic algorithm (see Fig. 5 of [18]), in which a macroscopic model is combined with a microscopic model. Thus, in each time step, the runner's overall macroscopic movement is computed and coupled with the microscopic dynamic behavior of the guiding contacts using routines of Matlab[®] version 2015a. Basic parameters of the drive used for numerical simulations are collected from [20] and listed in Table 1. The dynamic parameters of the actuators, which are depended on the radius of the ruby hemispheres, are referred from [14] and shown in Table 2. Additionally, the preload range and the actuation amplitude of the guiding contacts were set according to the experimental implementation in [10]. It is noticed that, for the case that the radius of the ruby hemispheres is of 0.25mm , the maximal level of the preload is only 0.5N . Simulations with higher levels of the preload would have no meaning since the experimental implementation proves that when the preload level is higher than 0.5N the drive does not work reliably anymore.

Table 3 shows variations of simulation parameters caused by the fabrication and assembly tolerance. In the standard case, on one side of the runner, the angle between two actuator blocks δ and the angle between two working surfaces of the runner γ are equal to 90° (see Figs. 6b and 7a, b). If the fabrication and assembly tolerance are considered, these parameters are varied according to the column "Varied value" of Table 3. Because the fabrication and assembly tolerance are random quantities, values of δ and γ can be smaller or larger than 90° . Also, the stiffness and the damping ratio of the actuators are varied to reduce to amounts of 10% and 20%, describing for the fabrication tolerance of the piezo and the inequality in the thickness of the glue layer. Based on these varied parameters, we perform dynamic simulations and compare results with that of the standard case. Consequently, discrepancies in percentage between the standard case and the varied cases are calculated and presented. Simulation cases are as follows:

- Case 1: The angle between two actuator blocks on one side of the runner (δ) is varied. The change is assigned to either Type-A side or Type-B side;
- Case 2: The angle between two working surfaces on one side of the runner (γ) is varied and the change can happen either on Type-A side or Type-B side;
- Case 3: The stiffness and damping ratio of actuators in one group (either the Type-A group with four actuators or the Type-B group with two actuators) are varied to reduce. Other parameters remain unchanged.

Table 1 Data used for numerical simulations [10, 20]

Parameters	Value
Young's modulus ruby - E_1 (GPa)	370
Young's modulus steel - E_2 (GPa)	210
Poisson's ratio - ν_1, ν_2	0.33
Friction coefficient - μ	0.3
Mass of the runner - m_r (g)	3
Stiffness of the load cell - k (N/m)	2.5×10^4
Radius of the ruby hemispheres - R (mm)	0.25, 0.5, 1

Table 2 Standard parameters dependent on the radius of hemispheres used in simulations [20]

Parameters	$R = 0.25 \text{ mm}$	$R = 0.5 \text{ mm}$	$R = 1 \text{ mm}$
Stiffness of actuators - k_p (N/m)	4×10^6	6×10^6	6.5×10^6
Damping ratio - c_p (kg/s)	10	14	16.3
Mass of actuator - m_a (g)	1.1×10^{-5}	1.6×10^{-5}	2.2×10^{-5}
Preload range - F_p (N)	$0.1 \div 0.5$	$0.1 \div 0.8$	$0.1 \div 1.5$
Actuation amplitude - A (nm)	96	160	200

Table 3 Parameter variation depending on the fabrication and assembly tolerance

Parameter	Position	Standard value	Varied value
Angle between two actuator blocks on one side of the runner (δ)	Type-A side Type-B side	$\delta = 90^\circ$	$\delta = 80^\circ/100^\circ, 70^\circ/110^\circ$
Angle between two working surfaces on one side of the runner (γ)	Type-A side Type-B side	$\gamma = 90^\circ$	$\gamma = 85^\circ, 95^\circ$
Stiffness and damping of the actuators (k_p, c_p)	Actuator 1, 2 Actuator 3, 4, 5, 6	From that of Table 2	k_p, c_p reduced 10% k_p, c_p reduced 20%

4. RESULTS AND DISCUSSION

In this section, the operational characteristics of the drive including the repeatability of the step length, the critical/0-amplitude phenomenon, and the maximal achievable driving frequency/velocity are analyzed. Based on the simulation results, discrepancies are shown and discussed. Also, some analytical formulations are presented.

4.1. The repeatability of the step length

Discrepancies of the step length depending on the preload when comparing the simulation results of the standard case with the varied cases (changing of δ and γ) are shown in Fig. 9., where Fig. 9a is for the case radius of the ruby hemispheres $R = 1 \text{ mm}$ and Fig. 9b for $R = 0.25 \text{ mm}$. It is seen in Fig. 9a that if γ or δ is varied, the discrepancy is increased with the rising level of the preload. When the preload is small, the discrepancy is very low and can be neglected. However, when the preload becomes higher, for example, 1.5 N , the maximum discrepancy reaches 7.5%. It is also clear that the influence of γ is larger than that of δ because the changing of γ leads to a change in both the actuation amplitude and the normal force, while the changing of δ changes only the actuation amplitude. The influence of δ is quite small and thus can be neglected.

Discrepancies of the step length depending on the preload when comparing the simulation results of the standard case with the case of reduced actuators stiffness and damping ratio are shown in Fig. 10 where Fig. 10a is for the case radius of the ruby hemispheres $R = 1 \text{ mm}$ and Fig. 10b for $R = 0.25 \text{ mm}$. A similar trend as in Fig. 9 is obtained. However, the discrepancy is smaller.

Comparing the simulation results from Figs. 9a and 10a with the experimental data in Fig. 3a, it is inferred that the simulation can cover the overall trend of the experiment where the discrepancy slightly increases with rising preloads. However, the level of changing in

simulations is still smaller than that of the experiment. A similar trend for the case $R = 0.25\text{mm}$ is observed.

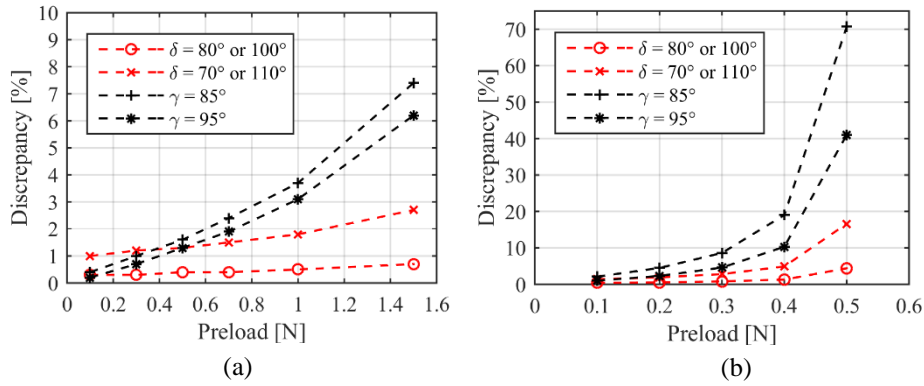


Fig. 9 Discrepancies of the step length depending on the preload when comparing the simulations with the standard case and the varied cases (changing of γ and δ): a) $R = 1\text{mm}$; b) $R = 0.25\text{mm}$

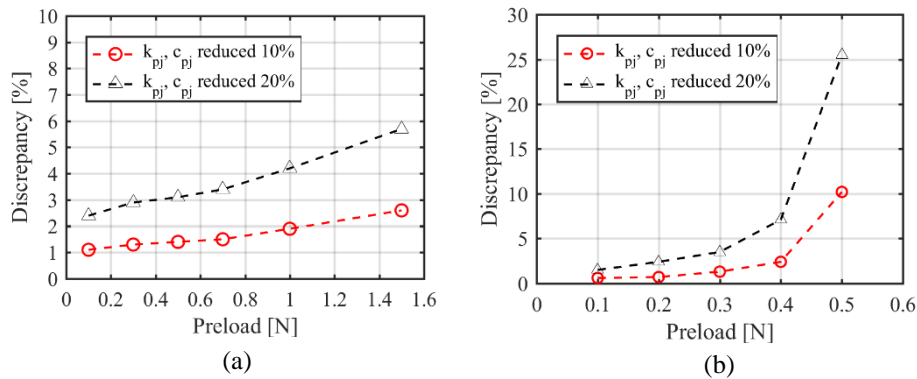


Fig. 10 Discrepancies of the step length depending on the preload when comparing the simulations with the standard case and the case with reduced actuators stiffness and damping ratio: a) $R = 1\text{mm}$; b) $R = 0.25\text{mm}$

It can be concluded that when the size of the system is reduced, the repeatability of the step length is decreased and the influence of the fabrication and assembly tolerance becomes more apparent with the increasing discrepancy. The fabrication tolerance of the runner has the strongest influence on the step length because it changes both the actuation amplitude and the normal contact forces.

4.2. The critical amplitude

The so-called “zero/critical-amplitude” phenomenon of PASSMDs was experimentally detected and modeled in previously published works [10, 14, 16, 18, 20]. If the actuation amplitude of the piezo elements is smaller than a critical value, no measurable step of the runner is achieved. The runner is only oscillated around its initial position without any generation of a net step. This phenomenon relates directly to the maximal tangential deformation of the guiding contact between the runner and the actuators and the tangential dynamic behavior of the piezo actuators. The state-of-the-art explanation for this phenomenon is presented in [20]. In this work, the influences of the fabrication and assembly tolerances of the system on this characteristic are analyzed. Based on the variation of the parameters in Table 3, simulations of the dependency of the critical amplitude on the preload were performed.

In Fig. 11a, discrepancies between simulation results of the standard case and the varied case ($\gamma = 85^\circ$) of the critical amplitude depended on the preload are shown. Two cases of the radius of the ruby hemispheres are considered. It is seen that, for both cases of the radius, the discrepancy varies from 2 to 7% for the overall preload range. This discrepancy qualitatively matched with the experimental data where the maximal values vary from 6.8 to 8.2% (see Fig. 4 and the corresponding text). Simulations for other varied cases (changes of δ , stiffness and damping ratio) show that the discrepancy is smaller and has a similar trend. For the sake of brevity, the results are not shown here. The obtained results can be explained based on the causation of the critical amplitude. If γ is changed, the normal contact force and the displacement amplitude of the contact point are changed, leading to a change in critical amplitude. For the case of changing of δ , only the displacement amplitude of the contact point is changed and thus, the changing of the critical amplitude is smaller. Similarly, for the case of reducing stiffness and damping ratio, a reduction of 10% or 20% does not much affect the stiffness and damping ratio because their values are still high. Therefore, less changing of the critical amplitude is achieved.

We come to the conclusions that for actuators with high stiffness, the influence of the fabrication tolerance on the critical amplitude is very small and can be neglected. The influence of δ is also small since it changes only the displacement amplitude of the contact point in a small amount proportional to the ratio A/A' .

In [20], analytical formulations (Eqs. (10) – (14) of [20]) for explaining the critical amplitude were established, which are an extension of Eq. (3.26) of [22] when considering the dynamic behavior of the actuators. The formulations fit excellently with experimental data. However, the formulations are established in an assumption that the behavior of an individual actuator in each actuator group is identical. No fabrication and assembly tolerance are considered. Thus, in this paper, we continue extending the formulations in such a way that influences of the tolerance are considered (see Eqs. (6) and (10) – (13)). In this extension, the critical amplitude is a function of the maximal tangential displacement of the guiding contacts $u_{x,max,j}$, the tangential deformation of the piezo $u_{x,a,j}$ under consideration of the interaction between the two actuator groups, where $j = 1$ for actuators of the Type-A side and $j = 2$ for actuators of the Type-B side. The influence of the tolerance of γ and δ on the changing of the displacement of the contacts is represented by factor A/A' in Eq. (12). Also, the change in normal forces is determined by Eq. (6). The reduction of the stiffness is modeled in Eq. (11). Fig. 11b shows the comparison of dynamic simulations of the critical amplitude depending on the preload and the analytical

approximation (13) for both cases of the radius of the ruby hemispheres. It is seen that the analytical approximations fit excellently with the dynamic simulations.

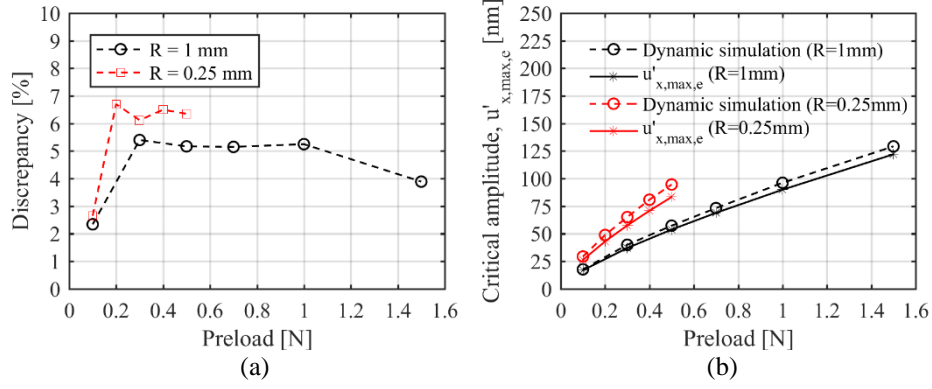


Fig. 11 Dependency of the critical amplitude on the preload: a) discrepancies between simulation results of the standard case and the varied case ($\gamma = 85^\circ$); b) comparison of dynamic simulation and analytical formation determined from Eqs. (6) and (10)–(13).

$$u_{x,max,j} = \frac{3\mu}{4G^*} \left(\frac{4E^*}{3} \right)^{1/3} \frac{F_{Nj}^{2/3}}{R^{1/3}} \quad (j=1, 2) \quad (10)$$

$$u_{x,a,j} = \mu \times \frac{F_{Nj}}{k_{pj}} \times \frac{m_r + m_a}{m_r} \quad (j=1, 2) \quad (11)$$

$$u'_{x,max,j} = \frac{A}{A} u_{x,max,j} + u_{x,a,j} \quad (j=1, 2) \quad (12)$$

$$u'_{x,max,e} = \frac{2u'_{x,max,1} u'_{x,max,2}}{u'_{x,max,1} + u'_{x,max,2}} \quad (13)$$

4.3. The maximal achievable driving frequency/velocity

One important characteristic of the drive is the maximal-achievable velocity of the runner, depending on the driving frequency. In fact, after each slip phase, there appear micro-vibrations of the overall system. If the micro-vibration cannot be damped before a new cycle of the stick and slip phase is started, it will induce chaos to the system. This prevents us from controlling the drive at high driving frequencies, influencing directly to the velocity of the runner. Thus, we can only drive the system at a maximal-achievable driving frequency. Above this frequency level, the velocity of the runner is reduced. The micro-vibration depends on the mechanics of the guiding contacts, the preload, and the dynamics of the piezo actuators, which is influenced by the fabrication and assembly tolerance. Fig. 12 shows a comparison of the maximal-achievable velocity of the runner

depending on the preload between the standard case and the varied cases. For each level of the preload, the value of the maximal-achievable driving frequency is shown.

It is seen in Fig. 12a that, for all cases, if the preload rises, the maximal-achievable driving frequencies and thus the maximal-achievable velocity of the runner is decreased. For the case with $\delta = 80^\circ$ or 100° only the displacement amplitude of the guiding contacts is slightly changed and thus, it will not influence significantly on the result when comparing with the standard case. The two plots of these cases are mostly identical. For the case $\gamma = 85^\circ$, the displacement amplitude of the guiding contacts is reduced, and the normal contact forces are increased. Compared to the standard case, this case leads to reductions of the maximal-achievable velocity of the runner with a maximal discrepancy of 6%. When both stiffness and damping ratio are reduced to 20%, the velocity is slightly increased. This can be explained that the reduction of the damping ratio leads to the increasing step length. This increasing level is larger than the decreasing step length caused by the reducing stiffness. Consequently, the final step length is increased, leading to an increment of velocity for the runner. The maximal discrepancy for this case is 4%.

Simulation results for the case with $R = 0.25mm$ are shown in Fig. 12b. A similar trend as in Fig. 12a is detected. The maximal discrepancy is 5%. However, the maximal-

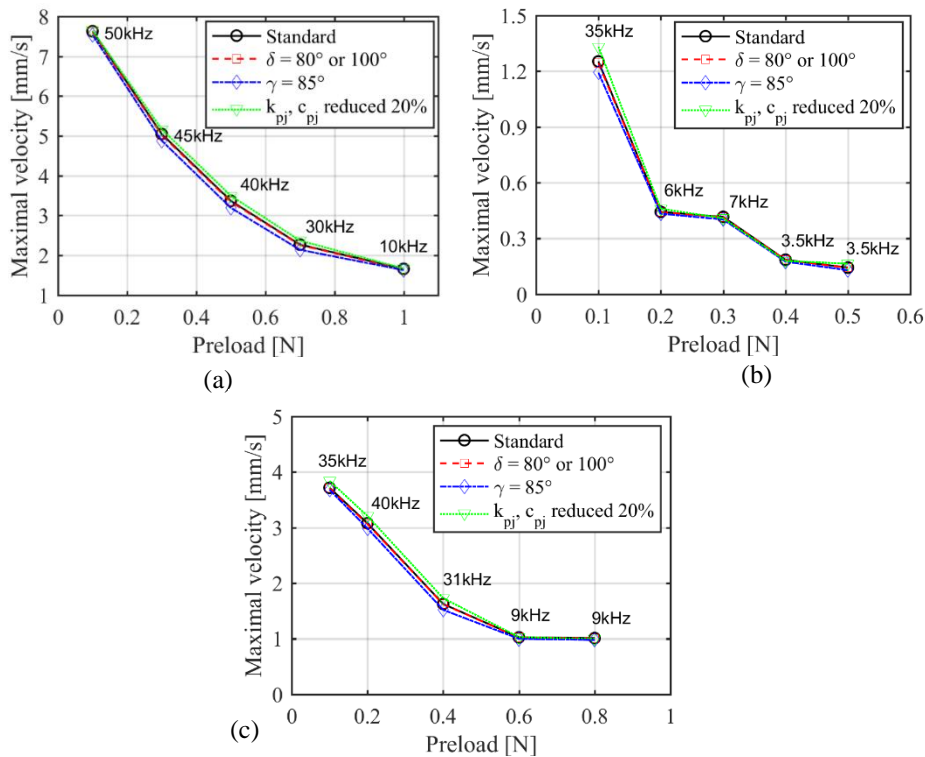


Fig. 12 Comparison of the maximal-achievable velocity of the runner depending on the preload between the standard case and the varied cases: a) $R = 1mm$; b) $R = 0.25mm$; c) $R = 0.5mm$

achievable driving frequency and thus the velocity of the runner is reduced significantly. Fig. 12c shows simulation results for the case $R = 0.5mm$. A similar trend is also obtained. At the preload $F_N = 0.4N$, the maximal-achievable velocity of the runner reaches $1.62mm/s$ at a maximal-controllable driving frequency of $31kHz$. When considering the influence of the fabrication and assembly tolerance, the maximal discrepancy is 6.4%. Compared to the experimental data shown in Fig.5, where the maximal velocity is $1.76mm/s$ at a driving frequency of $26kHz$ and the maximal discrepancy is of 7.4%, it is observed that the simulation fits very well with the experiment.

It can be concluded that the maximal-achievable driving frequency/velocity depends strongly on the size of the system. When the size of the system decreases, the maximal-achieve driving frequency/velocity as well as the repeatability reduce. The influence of the fabrication and assembly tolerance becomes larger.

5. CONCLUSION AND OUTLOOK

In this work, influences of the fabrication and assembly tolerance on operational characteristics of PASSMDs have been investigated for the first time. Three possible cases which are caused the fabrication and assembly tolerance are analyzed and chosen to investigate. Based on a PASSMD and a model of the previously published work, an extended model has been introduced. The model allows considering parameters representing influences of the fabrication and assembly tolerance. Under these influences, three important operational characteristics of the drive, including the repeatability of the step length, the critical amplitude and the maximal-achievable driving frequency/velocity have been evaluated via the more general hybrid-dynamic simulations.

It is concluded that the repeatability of the step length is clearly influenced by the fabrication and assembly tolerance. The discrepancy among step lengths is gradually increased if the preload rises and the size of the system is reduced. For all possible cases caused by the tolerance investigated in this paper, the influence of the fabrication tolerance of the runner represented by the angle γ is largest since it modifies not only the displacement amplitude of the contact point but also the normal contact forces. The influence caused by the assembly tolerance of the actuator block described by δ is less of impact. The changes in the stiffness and damping ratio of the actuator influence all the characteristics moderately. If the stiffness of the actuators is low, the influence becomes apparent. When the size of the system reduces, the influence of the fabrication and assembly tolerance on the driver's characteristics become larger.

The results of this work would be very helpful for the design and fabrication process of PASSMDs. Understanding causations resulting from the changes of operational characteristics and their influencing levels allows to optimize for better generation of PASSMDs. In the future, an optimization process for the design and fabrication of PASSMDs is planned to investigate.

REFERENCES

1. Chaillat, N., Régnier, S., 2010, *Microrobotics for Micromanipulation*, John Wiley and Sons Inc, USA, 484 p.
2. Pohl, D.W., 1987, *Dynamic piezoelectric translation devices*, Review of Scientific Instruments, 58, pp. 54-57.
3. Nguyen, H.X., 2014, *Simulation, Validation and Optimization of Stick-Slip Drives for Nanorobotic Applications*, PhD Thesis, Oldenburg University, Germany, 165 p.
4. Zhang, Z.M., An, Q., Li, J.W., Zhang, W.J., 2012, *Piezoelectric friction-inertia actuator-a critical review and future perspective*, Int J Adv Manuf Technol, 62, pp. 669-685.
5. Hunstig, M., 2017, *Piezoelectric Inertia Motors—A Critical Review of History, Concepts, Design, Applications, and Perspectives*, Actuator, 6(1), pp.7.
6. Bergander, A., 2003, *Control, Wear testing and Integration of Stick-Slip Micropositioning*, PhD Thesis, Ecole Polytechnique Federale de Lausanne, 171 p.
7. Qin, F., Tian, L., Huang, H., Wang, J., Liang, T., Zu, X., Zhao, H., 2019, *Actively controlling the contact force of a stick-slip piezoelectric linear actuator by a composite flexible hinge*, Sensors and Actuators A: Physical, 299, 111606.
8. Hunstig, M., Hemsell, T., Sextro, W., 2013, *Stick-slip and slip-slip operation of piezoelectric inertia drives. Part I: Ideal excitation*, Sensors and Actuators A: Physical, 200, pp. 90-100.
9. Hunstig, M., Hemsell, T., Sextro, W., 2013, *Stick-slip and slip-slip operation of piezoelectric inertia drives—Part II: Frequency-limited excitation*, Sensors and Actuators A: Physical, 200, pp. 79-89.
10. Nguyen, H.X., Teidelt, E., Popov, V.L., Fatikow, S., 2014, *Modeling and waveform optimization of stick-slip micro-drives using the method of dimensionality reduction*, Arch Appl Mech, 86, pp. 1771-1785.
11. Špiller, M., Hurák, Z., 2011, *Hybrid charge control for stick-slip piezoelectric actuators*, Mechatronics, 21(1), pp. 100-108.
12. Hunstig, M., Hemsell, T., Sextro, W., 2013, *Modelling the friction contact in an inertia motor*, Journal of Intelligent Material Systems and Structures, 24(11), pp. 1380-1391.
13. Van der Wulp, H., 1997, *Piezo-Driven Stages for Nanopositioning with extreme stability: Theoretical Aspects and Practical Design Considerations*, PhD Thesis, Technische Universiteit Delft, Netherlands.
14. Breguet, J.-M., 1998, *Actionneurs "Stick and Slip" pour Micro-Manipulateurs*, PhD Thesis, Ecole Polytechnique Federale de Lausanne, 152 p.
15. Peng, J.Y., Chen, X.B., 2011, *Modelling of piezoelectric-driven stick-slip actuator*, IEEE/ASME Transactions on Mechatronics, 16(2), pp. 394-399.
16. Edeler, C., 2011, *Modellierung und Validierung der Krafterzeugung mit Stick-Slip-Antrieben für Nanorobotische Anwendungen*, PhD Thesis, Oldenburg University, Germany, 187 p.
17. Popov, V.L., 2012, *Basic ideas and applications of the method of reduction of dimensionality in contact mechanics*, Physical Mesomechanics, 15, pp. 254-263.
18. Teidelt, E., Willert, E., Filippov, A.E., Popov, V.L., 2012, *Modelling of the dynamic contact in stick-slip microdrives using the method of reduction of dimensionality*, Physical Mesomechanics, 15, pp. 287-292.
19. Nguyen, H.X., Teidelt, E., Popov, V.L., Fatikow, S., 2014, *Dynamic tangential contact of rough surfaces in stick-slip microdrives: Modelling and validation using the method of dimensionality reduction*, Physical Mesomechanics, 17(4), pp. 304-310.
20. Nguyen, X.H., Mau, T.H., Meyer, L., Dang, B.L., Pham, H.P., 2018, *Improvements of piezo-actuated stick-slip micro-drives: Modelling and driving waveform*, Coatings, 8(2), 62.
21. Edeler, C., 2010, *Dynamic-mechanical analysis of piezoactuators for mobile nanorobots*, Messe Bremen conference, Germany.
22. Teidelt, E., 2014, *Oscillating Contacts Friction Induced Motion and Control of Friction*, PhD Thesis, Technische Universität Berlin, Germany, 131 p.